JACS
JOURNAL OF THE AMERICAN CHEMICAL SOCIETY
pubs.acs.org/JACS
Article

Understanding the Performance Gap between Polycrystalline and Single-Crystal Nickel-Rich Layered Oxide Cathodes

Jing Wang, Jinghao Huang, Weiyuan Huang, Haozhe Zhang, Tao Zhou, Qijia Zhu, Jingtian Yang, Tianyi Li, Lu Ma, Xianghui Xiao, Zengqing Zhuo, Jihyeon Gim, Gangbin Yan, Xiaozhou Huang, Matthew Li, Rachid Amine, Jianguo Wen, Tongchao Liu,* Ying Shirley Meng,* and Khalil Amine*

Cite This: https://doi.org/10.1021/jacs.5c18922

Read Online

ACCESS | Metrics & More | Article Recommendations | Supporting Information

ABSTRACT: Singe-crystal (SC) nickel-rich layered oxide cathodes, composed of boundary-free particles with high tap density, offer significant advantages in volumetric energy density and mechanical strength compared with polycrystalline (PC) cathode materials. However, as the nickel content increases (≥80%), SC Ni-rich cathodes often suffer from faster performance degradation than PC cathodes of the same composition, and the underlying causes of this discrepancy remain poorly understood. Herein, we reveal the distinct Ni redox behaviors that govern the electrochemical performance of SC and PC Ni-rich cathodes using multiscale and operando characterization techniques. Our results indicate that the increasingly heterogeneous Ni oxidation process in SC cathodes leads to the additional irreversible oxygen redox activity that deteriorates both the mechanical and chemical structures. In contrast, PC cathodes, despite with more pronounced surface reconstruction, exhibit greater chemomechanical stability due to homogeneous redox reactions during charging. Consequently, we find that bulk degradation, more than surface reactions, ultimately leads to fast capacity decay of SC Ni-rich cathodes during cycling. This work offers a comprehensive view on the impact of Ni redox evolutions on the chemomechanical stability in Ni-rich layered oxide cathodes, providing new insights into the longstanding performance gap between SC and PC cathodes, and guiding the rational design of Ni-rich cathode architectures.

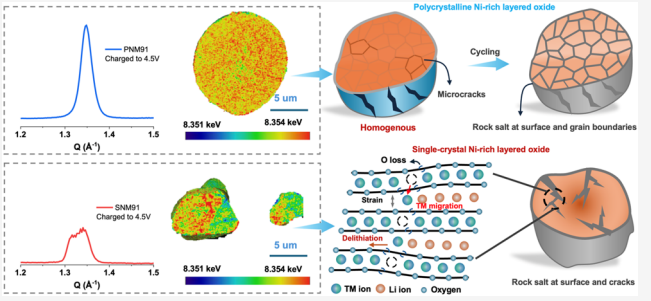

1. INTRODUCTION

The pursuit of a sustainable energy economy necessitates the advancement of lithium-ion batteries (LIBs) with high energy densities, which aims for 350 Wh/kg by 2025 and exceeds 400 Wh/kg by 2030.[1−3] Among various battery components, layered transition-metal oxide cathode materials are widely recognized as the primary determinants of battery energy density, cost, and safety, and have therefore become the focus of both academic and industrial research.[4,5] Especially, Ni-rich NMC ($LiNi_xCo_yMn_{1-x-y}O_2$, $x \geq 0.6$) have emerged as a near-consensus choice for electric vehicle batteries and offer a promising balance of capacity, cost efficiency, and cycling life.[6−10] To further boost energy density, Ni-rich NMC cathodes may increase the nickel content to unlock higher capacity by leveraging the Ni^{2+}/Ni^{4+} redox couple, or maximize the tap density for higher volumetric energy density.[11,12] SC Ni-rich NMC consisting of microsized boundary-free particles (1−10 μm in size) is one of the most promising cathode candidates for high-energy LIBs.[13−16] In addition to sharing the same intercalation/deintercalation chemistry with conventional polycrystalline Ni-rich cathodes (PC-NMC), the SC-NMC cathode can deliver a higher compact density (>3.5 g cm^{-3} vs ∼PC-NMC 3.2 g cm^{-3}).[17,18] The elimination of grain boundaries enhances mechanical robustness during electrode fabrication and electrochemical cycling, while achieving SC morphologies typically requires high-temperature calcination, which can induce structural defects that impact electrochemical performance. SC-NMC cathodes at lower nickel content (Ni ≤ 60%), such as NMC532 ($LiNi_{0.5}Mn_{0.3}Co_{0.2}O_2$) and NMC622 ($LiNi_{0.6}Mn_{0.2}Co_{0.2}O_2$), have already demonstrated enhanced electrochemical performance.[19−22] However, as the nickel content exceeds 80%, the advantages of the single-crystal configuration become less evident in both capacity and cycling stability.[23−26]

Typically, two primary sources have been identified in the degradation mechanisms arising from the high Ni content: surface reactivity and bulk instability.[27−30] The high-valence Ni species exhibited at high state of charge (SoC) tend to trigger parasitic reactions at the cathode/electrolyte interface, leading

Received: October 27, 2025
Revised: February 10, 2026
Accepted: February 11, 2026

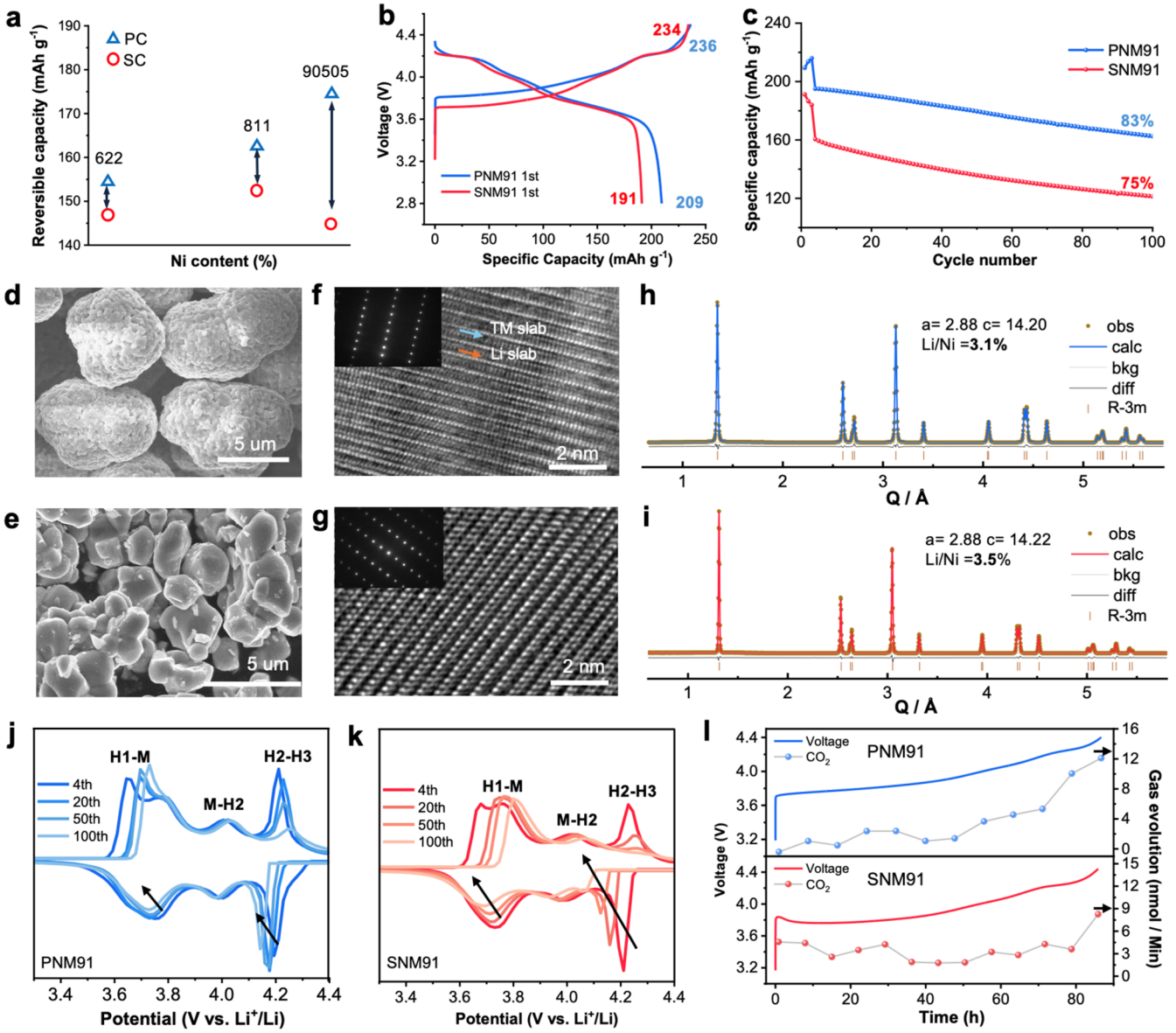

Figure 1. Structural properties and electrochemical measurements of the PC and SC cathodes. (a) Comparison on the reversible capacity of PC- and SC-NMC622, NMC811, and NMC90505 after 100 cycles with a voltage range of 2.8−4.5 V. (b) Charge/discharge curve comparison of PNM91 and SNM91 with voltage ranges of 2.8−4.5 V at a current rate of 0.1 C. (c) Cycling performance of PNM91 and SNM91 within a voltage range of 2.8−4.5 V (3 formation cycles at 0.1 C and 100 cycles at 0.5C). (d, e) SEM images of pristine powders of PNM91 (d) and SNM91 (e). (f, g) High-resolution TEM images of PNM91 (f) and SNM91 (g) particles with selected-area diffraction images. (h, i) High-energy XRD curve and Rietveld refinement results of PNM91 (h) and SNM91 (i). (j, k) dQ/dV curves at different cycles of PNM91 (j) and SNM91 (k) at a current rate of 0.5C. (l), In situ differential electrochemical mass spectroscopy measurements for PNM91 (top) and SNM91(bottom).

to electrolyte decomposition and rock salt (RS) phase generation and subsequent loss of electrochemical kinetics and structural integrity.[31,32] In the bulk, the higher Ni content typically accelerates the onset of the H2−H3 phase transition, which leads to lattice collapse and internal strain accumulation.[33−36] Collectively, these phenomena reveal that higher capacity, achieved by increasing Ni content, exacerbates both surface and bulk structures, resulting in pronounced degradation regardless of the particle morphology (SC or PC). Yet, prior understanding fails to explain the increased performance gap between SC and PC cathodes when increasing the Ni content (Ni > 80%). Specifically, Ni-rich SC-NMC often exhibits worse cycling stability, even when operated at a lower capacity compared to PC-NMC of the same composition.[25,26] This unexpected trend suggests that differences in lithium diffusion pathways and lengths between SC and PC architectures may influence redox dynamics, thereby altering the primary degradation mechanisms. Still, the relationship among crystalline architecture, Ni redox behavior, and surface/bulk degradation in Ni-rich cathodes remains insufficiently understood.

In this work, we conduct a systematic investigation of the Ni redox behaviors in both Ni-rich PC and SC cathodes across multiple length scales, explaining the origin of the performance gap between them. Distinct Ni redox behaviors in the two cathodes are observed through the operando phase and chemical observation during cycling, as well as multiscale characterization of electronic and atomic structures within

https://doi.org/10.1021/jacs.5c18922
J. Am. Chem. Soc. XXXX, XXX, XXX−XXX

particles. Specifically, SC cathodes exhibited increasingly heterogeneous Ni oxidation reactions within individual particles during charging, leading to the activation of additional oxygen redox activity. This degrading chemical environment exacerbates strain accumulation over cycling, ultimately driving the formation of intragranular cracks. Conversely, PC cathodes exhibited a gradually enhanced reaction homogeneity during charging due to the electrolyte penetration into the interior of secondary particles. Despite more severe surface reconstruction and parasitic reactions at the cathode−electrolyte interface, PC cathodes show better electrochemical stability and chemomechanical structures over cycling with fewer microcracks observed within individual particles. Our findings challenge the conventional emphasis on surface degradation as the dominant contributor to performance deterioration in SC Ni-rich layered cathodes. Instead, we identify the coevolution of lattice strain and heterogeneous redox reactions as the principal drivers of fast capacity decay. Our work highlights a critical but previously overlooked role of Ni redox behaviors in mechanical stability and electrochemical performance in Ni-rich cathodes, revealing the origin of the distinct performance gap in SC and PC cathodes.

2. RESULTS AND DISCUSSION

To illustrate the impact of increasing Ni content in the structural stability of PC and SC cathodes, we conduct a comparative analysis of the electrochemical performance of PC- and SC-NMC with varying Ni contents, specifically, $LiNi_{0.6}Mn_{0.2}Co_{0.2}O_2$ (NMC622), $LiNi_{0.8}Mn_{0.1}Co_{0.1}O_2$ (NMC811), and $LiNi_{0.9}Mn_{0.05}Co_{0.05}O_2$ (NMC90505). The charge−discharge profiles in Supporting Figure 1a−c demonstrate that capacity increases with rising Ni content up to 80% for both PC and SC cathodes. The PC and SC cathodes with same compositions achieve similar initial charge capacities at different Ni contents. Nonetheless, SC-NMC cathodes consistently deliver lower discharge capacities and Coulombic efficiency than PC cathodes, and the disparity grows as the Ni content increases. Specifically, the capacity differences for Ni contents of 60, 80, and 90% are 7.2, 9.8, and 21.6 mAh g^{-1}, respectively, indicating that increasing Ni content magnifies the reversible capacity difference between PC- and SC-NMC cathodes. Moreover, SC cathodes exhibit similar or, in some cases, inferior stability compared to PC cathodes, even though they are cycled at much lower capacities (Supporting Figure 1d−f). Over prolonged cycling, the reversible capacity gap between PC and SC cathodes widens further with higher Ni content (Figure 1a).

In Co-containing Ni-rich layered oxides, the $Co^{3+/4+}$ redox couple can activate at potentials similar to $Ni^{3+/4+}$ pairs and initiate lattice oxygen redox reactions at high potentials, which complicate the investigation on kinetics and contribution from Ni redox.[37,38] Focusing on Co-free Ni-rich cathodes enabled a clearer examination of the intrinsic Ni redox behavior across PC and SC structures. Therefore, the PC $LiNi_{0.9}Mn_{0.1}O_2$ (PNM91) and SC $LiNi_{0.9}Mn_{0.1}O_2$ (SNM91) with the same Co-free composition were synthesized through a conventional coprecipitation method followed by a solid-state calcination process (Methods).[39,40] Titration analysis confirms that both PNM91 and SNM91 contain relatively low and comparable levels of surface residual lithium species (Li_2CO_3/LiOH) (Supporting Figure 2a,b, Methods). As shown in Figure 1b, the initial charging capacities at a current rate of C/10 (define 1 C = 200 mA g^{-1}) were 236 and 234 mAh g^{-1} for PNM91 and SNM91, respectively, while SNM91 shows 18.2 mAh g^{-1} lower discharge capacity than PNM91 at the first cycle. The capacity disparity is further magnified along cycling, showing 27.2 and 31.9 mAh g^{-1} at the second and third activation cycles, respectively, which indicates the different structure changes during cycling in the two samples (Supporting Figure 3a,b). Despite a significantly lower capacity, SNM91 presents a more severe capacity degradation than PNM91. As shown in Figure 1c, the capacity retentions over 100 cycles are recorded as 83 and 75% for PNM91 and SNM91, respectively. Clearly, the absence of Co exacerbates the degradation of SC cathodes compared to SC-NMC90505 (~81% capacity retention) and magnifies the impact of Ni on long-term structural stability. Full cells incorporating high-loading PNM91 and SNM91 cathodes (2 and 3 mAh cm^{-2}, respectively) show a similar trend, with PNM91 maintaining higher capacity and superior cycling retention (Supporting Figure 4).

Given the distinct electrochemical performances of PNM91 and SNM91, it was of particular interest to compare their initial morphologies and crystal structures. Scanning electron microscopy (SEM) images (Figure 1d) show that as-synthesized PNM91 exhibits a polycrystalline morphology, with secondary particle sizes ranging from 8 to 10 μm, composed of nanosize primary particles. In contrast, as shown in Figure 1e, SNM91 exhibits "single-crystal" morphology with particle sizes between 2 and 4 μm. High-angle annular dark-field scanning transmission electron microscopy (HAADF-STEM) images (Supporting Figure 5a,b) further confirm the presence of internal grain boundaries within PNM91 particles, while no domain boundaries are observed in SNM91. Aberration-corrected high-resolution transmission electron microscopy (TEM) coupled with selected-area electron diffraction (SAED) indicates the typical layered structures of the two samples, as illustrated in Figure 1f,g. The atomic-level inspection reveals a small number of weak signals within Li layers, suggesting the existence of Li/Ni antisite disorder. Additionally, the Rietveld refinement of synchrotron-based high-energy X-ray diffraction (HEXRD) data (Figure 1h,i) confirms that both PNM91 and SNM91 show a α-$NaFeO_2$-type layered structure with the $R\bar{3}m$ space group. As indicated in Supporting Tables 1 and 2, the Li/Ni disorders in PNM91 and SNM91 are calculated to be 3.1% and 3.5%, respectively. Based on the above observations, the similar initial crystal structures of PNM91 and SNM91 are unlikely to account for their distinct cycling behaviors.

As shown in Figure 1j,k, the dQ/dV curves of PNM91 and SNM91 both show three distinct peaks around 3.7, 4.0, and 4.2 V, corresponding to the H1−M, M−H2, and H2−H3 phase transitions, respectively.[41] During long-term cycling, PNM91 primarily demonstrates a gradual decline and voltage shift in the H2−H3 phase transition with minimal degradation observed in the other phase transitions. In contrast, SNM91 exhibits simultaneous decay across all dQ/dV peaks, accompanied by substantial peak shifts, indicating a distinct mode of structural degradation compared to that of PNM91.

Capacity decay in Ni-rich cathodes is generally attributed to electrolyte decomposition at high voltage, surface reconstruction of cathodes, and mechanical degradation from microcrack formation, or a combination of these factors.[42] Identifying the predominant degradation mode is essential for developing targeted interventions to improve battery cycle life, capacity retention, and safety, ultimately advancing the commercial viability of high-energy LIBs. To gain insights into the

https://doi.org/10.1021/jacs.5c18922
J. Am. Chem. Soc. XXXX, XXX, XXX−XXX

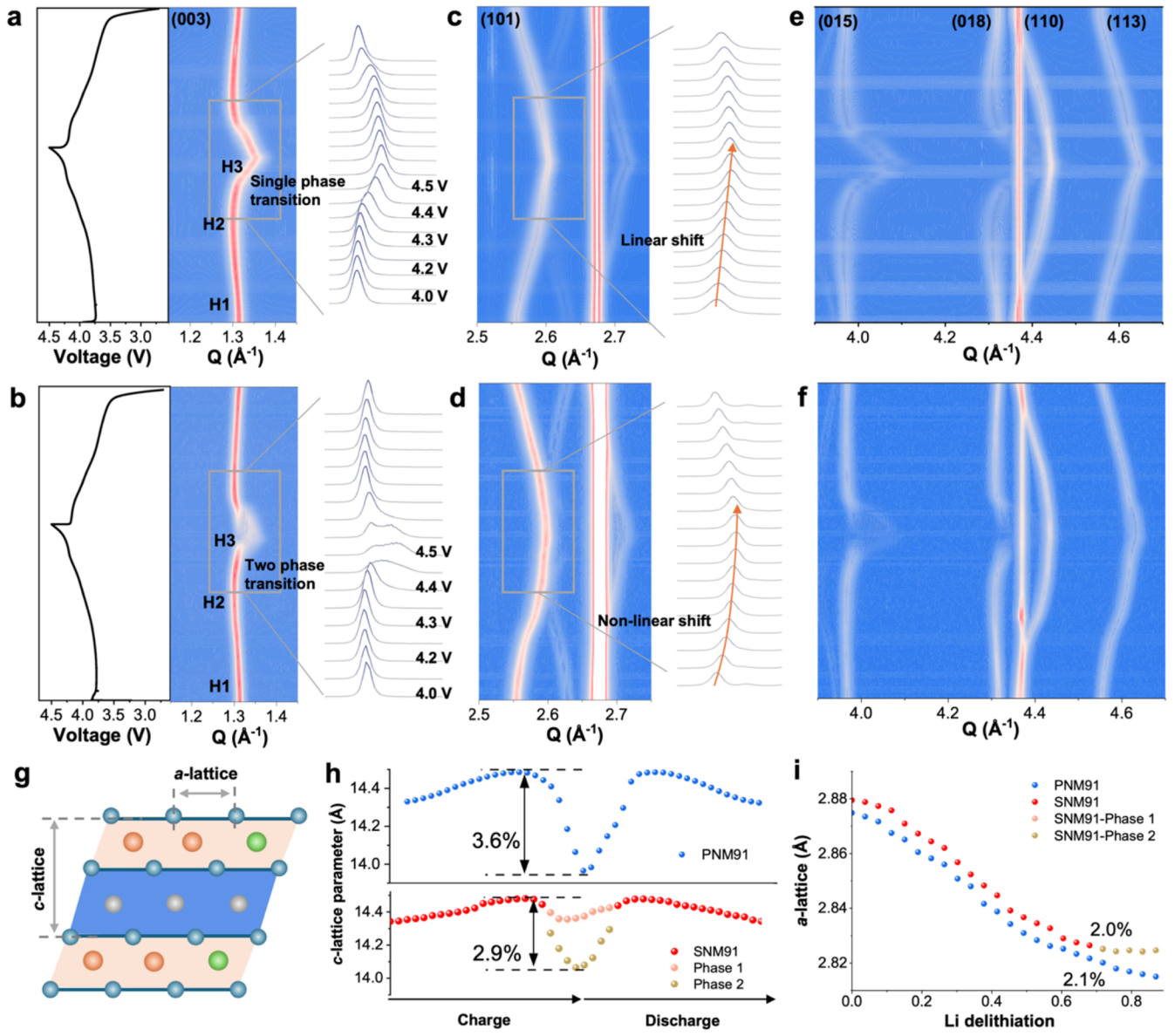

Figure 2. Structural evolutions of SNM91 and PNM91. (a, b) Charge−discharge profiles at the first cycle and corresponding evolution of the (003) reflection for PNM91 (a) and SNM91 (b). (c, d) Evolution of the (101) reflection for PNM91 (c) and SNM91 (d). (e, f) Evolution of the (015), (018), (110), and (113) reflections for PNM91 (e) and SNM91 (f). Electrochemical tests were performed within the voltage window of 2.7−4.5 V at a current density of 0.1 C. (g) Schematic diagram with typical lattice parameters (*a*- and *c*-axis) of layered oxide materials. (h, i) The *c*-axis lattice parameter changes (h) and *a*-axis parameter changes (i) of PNM91 and SNM91 obtained from Rietveld refinements. Two-phase refinements were conducted for SNM91 at high SoCs.

degradation mechanisms of PNM91 and SNM91, operando differential electrochemical mass spectrometry (DEMS) was carried out to compare their surface reactivities at the cathode−electrolyte interface. First, there was no evidence of direct O_2 generation during the charging process for both samples, with only a small amount of CO_2 detected. Interestingly, the generation of CO_2 occurred earlier and in larger quantities in PNM91 than in SNM91 at high potentials, despite the higher ICE and better cycling stability of PNM91 (Figure 1l). To further evaluate the surface stability, a 4.5 V float-test leakage current (Supporting Figure 6) was measured. The quasi-steady-state leakage current comparison confirms that surface side reactions were more prevalent in PNM91 than in SNM91. Additional cycling tests using a common electrolyte additive of 2% vinylene carbonate (VC) were conducted to evaluate the influence of interfacial stabilization on the PNM91 and SNM91 cathodes. Long-term cycling tests indicate that interfacial stabilization slightly improves the cycling stability of PNM91, with little effect on SNM91 (Supporting Figure 7). Together with the DEMS and leakage current measurement, the results indicate that the performance decay of SNM91 may not arise from the surface side reaction, indicating the need for an in-depth investigation on the bulk structure evolution.

In situ HEXRD measurements were performed on PNM91 and SNM91 to elucidate the phase-transition processes and their impact on structural evolution. Figure 2a,b shows the (003) peak evolutions for PNM91 and SNM91. The (003) peaks for both cathodes shifted initially to a lower angle upon charging to ~4.0 V, corresponding to phase transition from H1 to H2. The *c*-axis expansion during H1−H2 phase transition is

https://doi.org/10.1021/jacs.5c18922
J. Am. Chem. Soc. XXXX, XXX, XXX−XXX

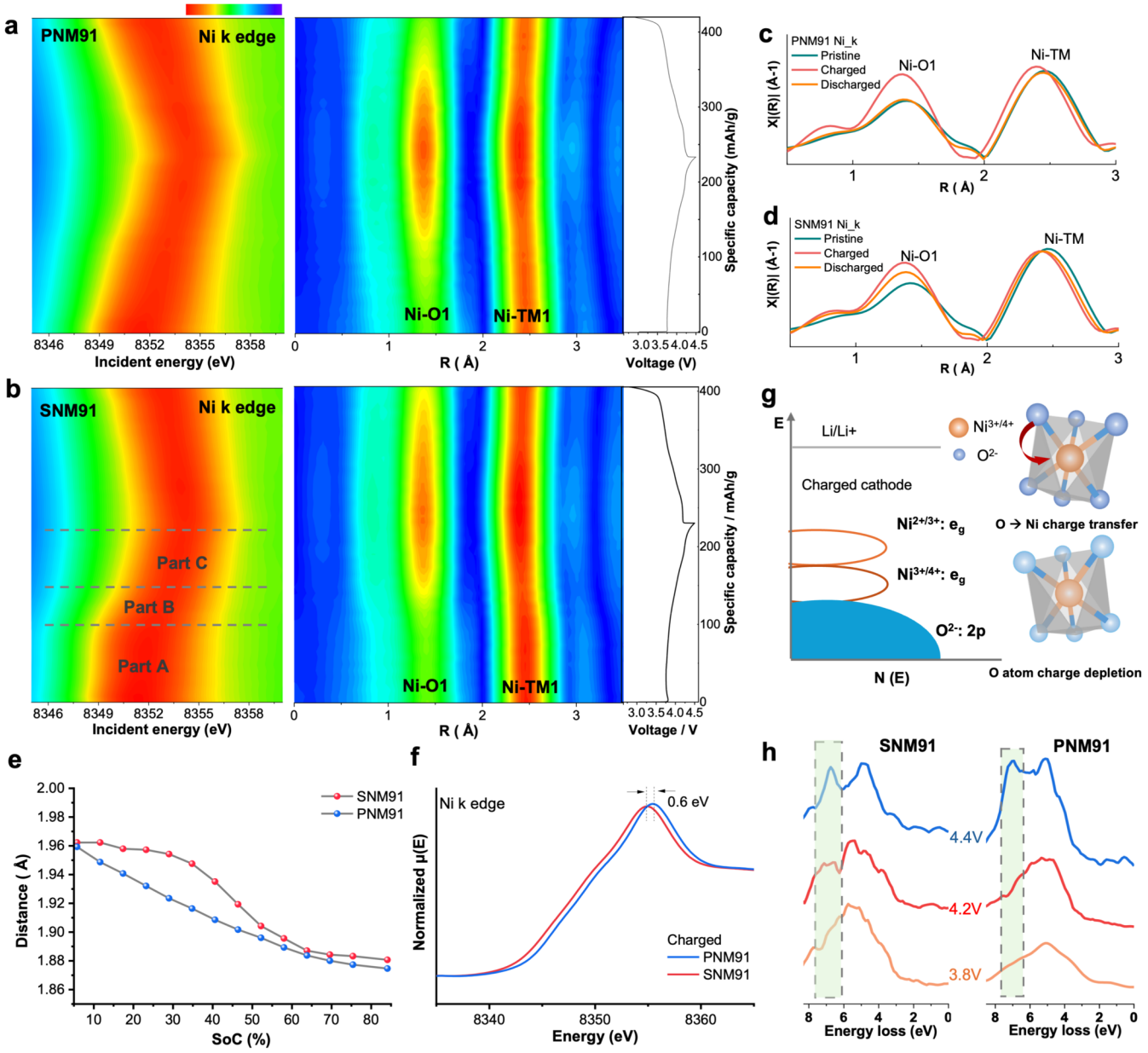

Figure 3. Chemical structure evolution of SNM91 and PNM91 at the first cycle. (a, b) In situ XANES and EXAFS spectra of the Ni K-edge and the corresponding voltage profiles of PNM91 (a) and SNM91 (b) during charge/discharge at 0.2 C. (c–d) Selected EXAFS spectra at different potentials for PNM91 (c) and SNM91 (d). (e) The Ni–O1 bond length and Debye–Waller factor of PNM91 and SNM91 cathode as a function of SoC, collected from the fitting of corresponding EXAFS spectra with a sample size of 14. (f) Comparison of Ni valence state at the end of charge. The electrochemical tests were performed within the voltage window of 2.7–4.5 V at a current density of 0.1 C. (g) Density of states schematic diagram of TMs and (h) RIXS line scans at an excitation energy of ~531 eV for SNM91 and PNM91 charged at different potentials.

attributed to the reduced electrostatic "shielding" between the negatively charged oxygen layers with delithiation.[43] After further charging to 4.5 V, the (003) peaks shift back to higher angles, which indicates lattice contraction along the *c*-axis as a phase transition to H3. As Ni is oxidized to higher valence states, the electrostatic attraction between the oxygen anions and Ni cations increases, resulting in *c*-lattice shrinkage.[36] During charge/discharge, PNM91 maintains a single-phase transition without showing any observable peak separation, indicating a homogeneous crystal structure change. Additionally, PNM91 exhibits a symmetric structural evolution during the first cycle, with diffraction peaks returning nearly to their original 2θ positions upon discharge, indicating minimal residual strain and good structural reversibility. However, the (003) peaks of SNM91 exhibit substantial peak broadening starting from 4.3 V. After discharge, the (003) peak deviated from its original peak position, suggesting an irreversible structural evolution during the first cycle.

The a/*b*-axis lattice parameter change indicated from (101) or (110) reflection is closely linked to the oxygen–oxygen (O–O) bond lengths and the oxidation states of transition metals (TMs).[36,44] As indicated in Figure 2c,d, both cathodes exhibit a shift of (101) reflection to higher angles upon charging, suggesting the continuous contraction of Ni–O bonds due to the oxidation of Ni. Notably, the evolution of (101) reflections varies slightly between the two cathodes: PNM91 shows a linear peak shift, indicating a smooth correspondence with the SoC during charging. However, it

https://doi.org/10.1021/jacs.5c18922
J. Am. Chem. Soc. XXXX, XXX, XXX–XXX

was observed that the a/*b*-axis lattice parameters of SNM91 show a sluggish shift at high potentials (above 4.3 V), which is different from the trend observed in PNM91. This behavior is likely linked to the significant (003) peak broadening in SNM91 at high delithiation, where it shows the coexistence of less-contracted and more-contracted phases within the structure. Similar phenomena are observed in (015) and (110) reflections indicated in Figure 2e,f. To quantitatively analyze lattice heterogeneity, the fwhm (full width at half-maximum) of the (003) peaks were calculated for both cathodes. As shown in Supporting Figure 8, the SNM91 exhibits a pronounced increase in lattice asymmetry during the H2−H3 phase transition, while PNM91 shows a relatively similar fwhm throughout the charging process. The broad fwhm indicates a more heterogeneous lattice structure and more significant microstrain within SC particles at high potentials.

Rietveld refinements of the in situ XRD data were performed to quantitatively track the *a*- and *c*-lattice parameter changes in both cathodes (Figure 2g−i, Supporting Figures 9, 10). The results indicate a slightly larger *a*-lattice change for PNM91 compared to SNM91 during charging, despite their similar capacities. Additionally, SNM91 shows a sluggish change of *a*-lattice parameter at high potentials, suggesting the potential existence of O redox activity by increased TM−O covalency.[42] The *c*-lattice collapse during the delithiation process typically occurs due to reduced repulsion between NiO_2 layers arising from either increased Ni oxidation or electron-deficient O^- formation. The maximum shift of the (003) peak in PNM91 is larger than that observed in SNM91 at the end of charge (Figure 2h and Supporting Figure 11), while the cycling stability of PNM91 is much better than that of SNM91. This suggests that the lattice parameter change is no longer applicable to indicate the structural stability between PC and SC cathodes. Instead, the presence of both less-contracted and more-contracted phases in SNM91 may contribute to more pronounced performance degradation. The less-contracted phase may stem from sluggish Ni oxidation, while the more-contracted phase reflects relatively increased covalency in the TM−O bond as corresponding to the sluggish change of the *a*-lattice parameter. In-depth investigation into the chemical-state change is further required to get insight on the different structural evolutions between PNM91 and SNM91.

In situ X-ray absorption spectroscopy (XAS) was conducted to further probe the dynamic chemical structure changes during the initial charge−discharge cycle in PNM91 and SNM91. The X-ray absorption near-edge structure (XANES) results (Figure 3a and Supporting Figure 12) show a gradual shift of the Ni K-edge to higher energies for PNM91 during charging, indicating progressive Ni oxidation. Concurrently, the extended X-ray absorption fine structure (EXAFS) reveals a reduction in Ni−O1 distances, which correlates with the increased Ni oxidation state (Supporting Figure 13). PNM91 exhibits a nearly linear increase in Ni valence accompanied by a corresponding decrease in Ni−O bond distance during charging, which is consistent with the linear decrease in the length of the O−O bond observed in the in situ XRD.

In contrast, SNM91 exhibits a nonlinear Ni K-edge shift that corresponds with its nonlinear (101) peak shift in XRD. As indicated in Figure 3b and Supporting Figures 14, 15, the Ni K-edge shift in SNM91 during charging can be segmented into three stages: Part A (OCV−3.8 V, < 35% SoC, where 100% SoC corresponds to 270 mAh g^{-1}) displays a gradual energy increase; Part B (3.8−4.0 V, 35−64% SoC) exhibits a rapid shift; and Part C (4.0−4.5 V, 64−85% SoC) shows a slower shift than part B. Upon discharge, the overall Ni valence in SNM91 remains higher compared to the initial state, suggesting the irreversible Ni redox activity. However, unlike SNM91, the Ni K-edge of PNM91 returns to its initial position with its coordination environment resuming to its original state, showing good Ni redox reversibility (Figure 3c−d and Supporting Figure 16). Distinct Ni oxidation behaviors between PNM91 and SNM91 are further highlighted in Figure 3e and Supporting Tables 3, 4, which illustrates Ni−O bond length variations as a function of SoC. To better understand the nonlinear shift of the Ni K-edge in SNM91, XANES spectra were compared with those of Ni^{2+} of Ni(II)O and Ni^{3+} of $LiNi(III)O_2$ standards (Supporting Figure 17). Given the instability of Ni in the +4 oxidation state, the Ni K-edge spectra for PNM91 at 4.5 V served as a reference for a valence close to +4. These comparisons indicate that Part A exhibits the shift from Ni^{2+} to Ni^{3+}, which is subtle, while the shift from Ni^{3+} to Ni^{4+} represented in Parts B and C is more pronounced. Therefore, the nonlinear Ni K-edge evolution observed in SNM91 can be attributed to the sequential nature of the $Ni^{2+}\rightarrow Ni^{3+}$ and $Ni^{3+}\rightarrow Ni^{4+}$ oxidation processes. However, the polycrystalline architecture of PNM91 may promote grain separation and electrolyte penetration due to the anisotropic volume change during delithiation. Thus, this may enable the $Ni^{2+}\rightarrow Ni^{3+}$ and $Ni^{3+}\rightarrow Ni^{4+}$ oxidations to occur concurrently across different primary grains, leading to the different Ni oxidation change processes from SNM91.

Interestingly, both cathodes exhibit nearly identical capacity and cycling stability at a cutoff voltage of 4.0 V (without undergoing Part C), implying that the cycling at low SoCs does not account for the performance discrepancies between them (Supporting Figure 18). As delithiation proceeds in Part C, the Ni oxidation rate slows especially for SNM91, likely arising from the kinetics limitation at the high delithiation state. Moreover, despite similar capacity in both cathodes, the shift of the Ni K-edge in SNM91 remains approximately 0.6 eV lower than in PNM91 at the end of charge, indicating an additional capacity contributor in SNM91 (Figure 3f). As shown in Supporting Figure 19a−d, no significant change of Mn K-edges in XANES was observed for both samples. Given the electrochemical inert properties for Mn^{4+}, it suggests that O may be involved in the redox at high potentials because its redox activity overlaps with $Ni^{3+/4+}$ pairs (Figure 3g). To probe this, resonant inelastic X-ray scattering (RIXS) at the O K-edge was performed, providing sensitivity to oxygen states at depths of ∼100 nm. As shown in Figure 3h, RIXS line scans were collected for SNM91 and PNM91 at different charge states (3.8, 4.2, and 4.4 V). For SNM91, the RIXS spectra at around 531 eV excitation reveal a broad inelastic feature at ∼7.5 eV, which is characteristic of oxidized O−O species (e.g., molecular O_2 or peroxo-like dimers) commonly observed in Li-rich and Ni-rich cathodes.[45,46] This feature becomes more pronounced at 4.4 V, indicating increased oxygen redox activity at high SoC (i.e., higher Ni oxidation states). In contrast, for PNM91, the inelastic feature emerges only at 4.4 V, suggesting a more stable oxygen environment. It is imperative to investigate the redox behaviors at the particle level to understand why SNM91 activated oxygen charge compensation at a lower potential compared to PNM91.

To build a relationship between chemical-state changes at the bulk and particle level, full-field transmission X-ray

https://doi.org/10.1021/jacs.5c18922
J. Am. Chem. Soc. XXXX, XXX, XXX−XXX

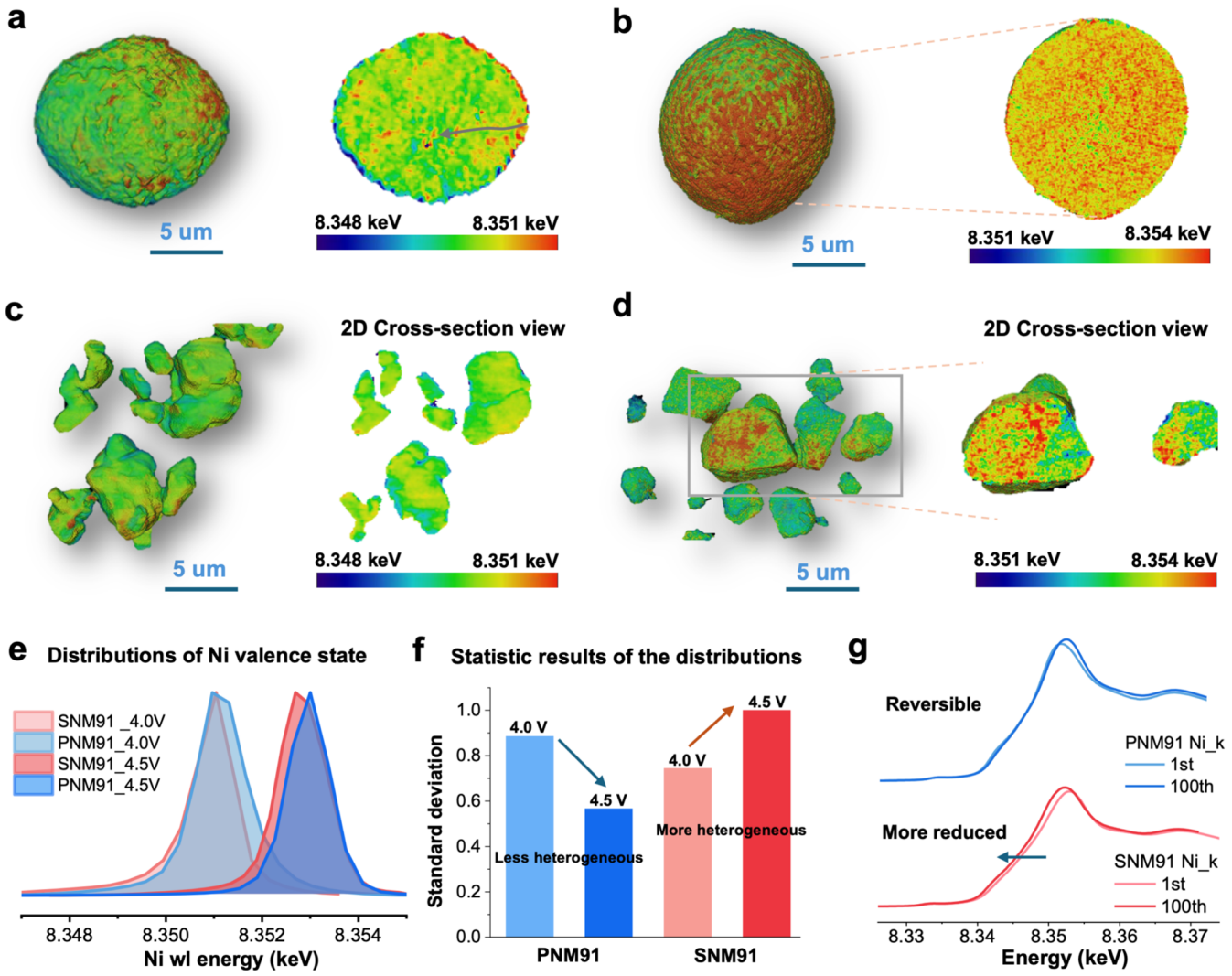

Figure 4. Observation on chemical oxidation states distribution. (a–d) The 3D renderings and cross-section views of Ni valence-state distribution for PNM91 at 4.0 V (a) and 4.5 V (b), and for SNM91 at 4.0 V (c) and 4.5 V (d), respectively. (e) Statistical average white-line energy distribution profiles of PNM91 and SNM91. (f) The standard deviation of the statistic results of the Ni valence distribution based on results from panel (e). (g) Ex situ Ni K-edge XANES spectra of PNM91 (top) and SNM91 (bottom) after the 1st cycle and 100th cycle.

microscopy (TXM) coupled with 3D XANES was further conducted to analyze the origin of different Ni redox evolutions in PNM91 and SNM91 cathodes. Figure 4a,c shows the Ni oxidation-state distribution (manifested by different colors) for charged PNM91 and SNM91 at 4.0 V, based on the white-line (WL) energy shift of Ni K-edge. In PNM91, a heterogeneous distribution of Ni valence states is evident across both the particle surface and cross section. Higher Ni valence species are observed not only on the particle surface but also within the interior, suggesting different reaction depths due to the existence of grain boundaries and potential electrolyte penetration. This aligns with the concurrent $Ni^{2+} \rightarrow Ni^{3+}$ and $Ni^{3+} \rightarrow Ni^{4+}$ oxidation processes of PNM91 indicated by in situ XAS. In contrast, SNM91 exhibits a relatively homogeneous Ni redox behavior in single particles at low SoC.

Figure 4b,d shows the Ni oxidation-state distribution for PNM91 and SNM91 when charged to 4.5 V. Unlike the heterogeneous distribution observed at 4.0 V, PNM91 exhibits a relatively uniform Ni oxidation state at 4.5 V, with a more homogeneous Ni valence distribution across the particle, as seen in the cross-sectional image (Figure 4b). In contrast, SNM91 shows an inhomogeneous Ni oxidation profile, indicating the presence of Ni species with varying valences within a single particle at the end of charge (Figure 4d). Statistical analysis of each 3D data set is presented in histograms (Figure 4e,f) for PNM91 and SNM91. The mean peak position corresponds to the average SoC within the particles: a lower WL energy reflects a less oxidized Ni state, while the shape and width of the peak indicate the heterogeneity in the SoC distribution. SNM91 demonstrates a lower average WL energy compared with PNM91, aligning with the electrode-level XAS data. Interestingly, a sharper peak is observed for SNM91 at 4.0 V compared to that of PNM91. However, as the potential increases, SNM91 displays a broader WL distribution, indicating an increased reaction heterogeneity within the particle at higher SoCs. The homogeneity observed at lower SoCs could be attributed to good Li diffusion kinetics and lower reaction resistance, as indicated in the GITT analysis (Supporting Figure 20). However, as charging progresses, the reaction in SNM91 becomes more heterogeneous, likely due to the pronounced lattice mismatch between the H2 and H3

https://doi.org/10.1021/jacs.5c18922
J. Am. Chem. Soc. XXXX, XXX, XXX−XXX

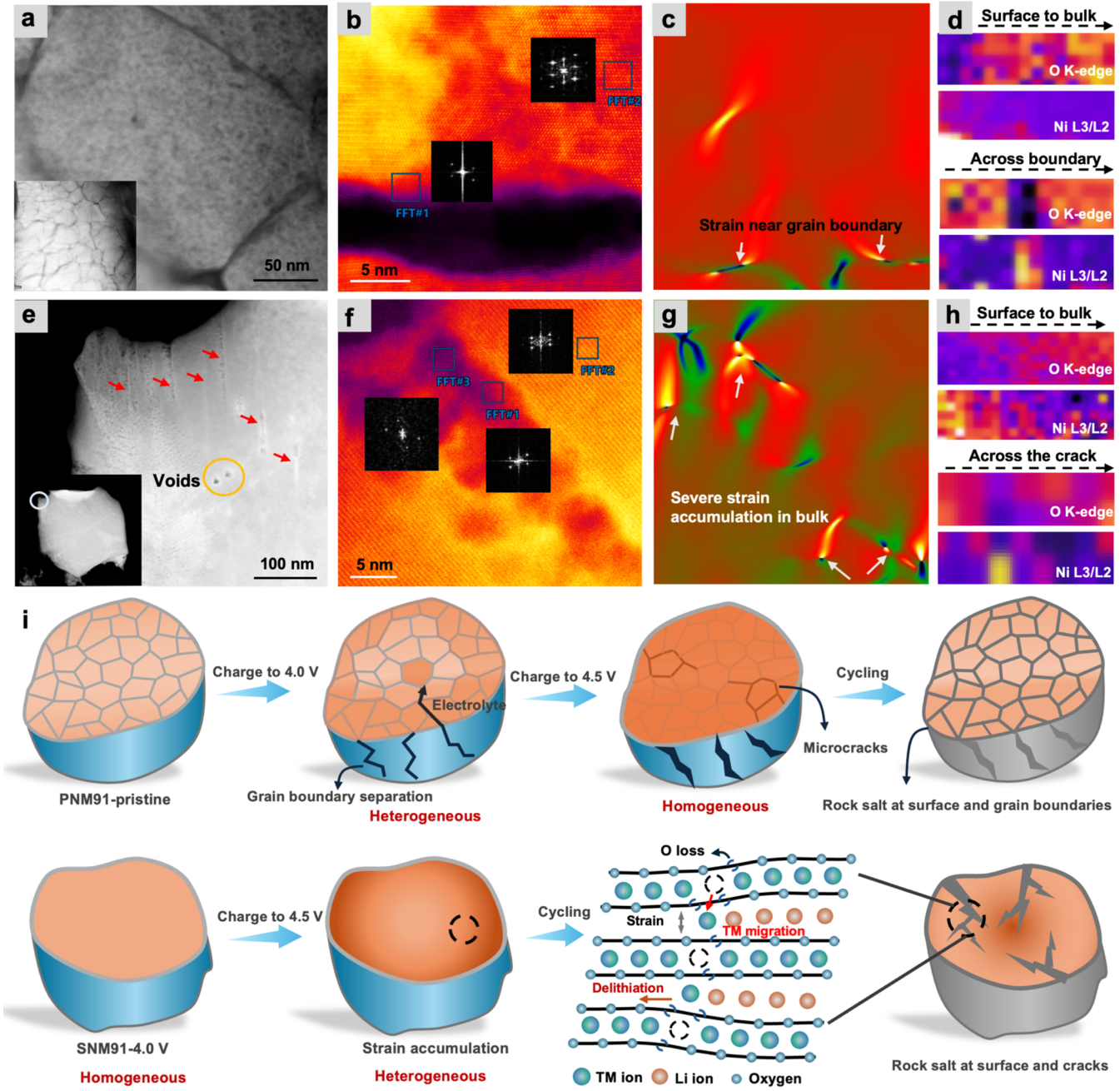

Figure 5. Observation of local chemical and structural changes after cycling. (a) TEM image of the PNM91 particle after 100 cycles. (b) High-resolution TEM images of PNM91 at the region of the grain boundary. Inserted figures are the SAED patterns collected near the grain boundaries (FFT #1) and at the bulk area (FFT#2), respectively. (c) Strain state in PNM91 observed by GPA. (d) EELS mapping of the O K-edge, and Ni L3/L2 from the surface to bulk (top) and across the grain boundary (bottom). Bright and dark colors represent high and low content in O K-edge mapping. The bright and dark colors indicate high and low L3/L2 intensity ratios in Ni L3/L2 mapping, respectively. A high L3/L2 ratio corresponds to a lower Ni valence state. (e) TEM image of SNM91 particles after 100 cycles. (f) High-resolution TEM images of SNM91 across intragranular cracks. Inserted figures are the SAED patterns collected near the microcrack (FFT #1), at the bulk area (FFT #2), and near the surface (FFT #3). (g) Strain state in SNM91 observed by GPA. (h) EELS mapping of the O K-edge, and Ni L3/L2 from the surface to bulk (top) and across the crack (bottom). (i) Schematic illustration of structural degradation of PNM91 and SNM91 cathodes.

phases. The increased layer contraction in the H3 phase may hinder Li diffusion within the lattice, leading to a rapid decline in the Li diffusion rate. Consequently, the structure becomes increasingly heterogeneous in SNM91 when charging to 4.5 V. In contrast, PNM91 shows reduced heterogeneity with an increase in the voltage. This behavior in PNM91 may be attributed to the electrolyte penetration through grain boundaries to the interior due to the sudden volume shrinkage at high SoCs. This observation is consistent with the in situ XRD and XAS results, where SNM91 displays clear H2−H3 phase separation and nonuniform Ni redox evolution at a high voltage, while PNM91 maintains single-phase behavior and linear Ni valence progression due to grain-boundary-mediated Li transport.

Moreover, it is confirmed by TXM-XANES that SNM91 shows a lower Ni oxidation state than PNM91 at the end of

https://doi.org/10.1021/jacs.5c18922
J. Am. Chem. Soc. XXXX, XXX, XXX−XXX

charge, despite both cathodes demonstrating nearly identical charging capacities. This suggests a greater contribution from charge compensation from oxygen in SNM91, which is caused by heterogeneous Ni oxidation within particles. The observed chemical and phase heterogeneity in SNM91 indicates a severe lattice mismatch, which destabilizes the structure and promotes oxygen release from the bulk. This oxygen release, in turn, triggers an irreversible structural change during cycling.

As shown by XAS data comparing Ni oxidation after the first cycle and the 100th cycle (Figure 4g), PNM91 maintains good Ni redox reversibility, even with a higher average Ni valence during cycling. In contrast, the overall Ni valence in the cycled SNM91 cathode appears to be reduced, which may be attributed to the gradual rock salt formation. As shown in Supporting Figure 21, cycled SNM91 cells experience more significant transition-metal dissolution (primarily Ni and Mn) and cross-contamination, which accelerates surface reconstruction on the cathode and significantly alters the composition and structure of the anode solid electrolyte interphase (Supporting Figure 22), leading to accelerated cell degradation. In contrast, PNM91 cells exhibit less Ni and Mn dissolution after extended cycling despite higher average Ni valence and more surface side reactions during charging. These findings indicate that the transition-metal loss in SNM91 primarily arises from bulk structural degradation associated with an irreversible lattice oxygen activity.

Morphological observations by SEM and TEM reveal that intergranular cracks were observed along the grain boundaries of PNM91 after long-term cycling (Figure 5a and Supporting Figure 23). It indicates the inevitable grain separation in the secondary particles due to the intrinsic anisotropic lattice change (i.e., expansion along the c direction and contraction along the a/b direction) during delithiation/lithiation.[47−49] The intergranular fracture allows electrolyte penetration to the newly exposed surface at the interior of the particles and induces surface phase transformation, as indicated by the inserted selected-area electron diffraction (SAED). As indicated in Figure 5b and Supporting Figure 24, the rock salt phase formed not only at the surface of PC particles but also along grain boundaries. However, the inner lattice of PNM91 maintains a stable layered structure, without observable microcracks, which indicates the stable lattice of Co-free Ni-rich cathodes by minimizing anionic redox reaction that can be exacerbated by Co−O charge compensation. The geometric phase analysis (GPA) reveals minor lattice distortions localized at grain boundaries, while the bulk lattice shows minimal distortion overall (Figure 5c). Detailed EELS mapping of the selected area (marked by the red and yellow rectangles in Supporting Figure 25) uncovered oxygen loss at the surface and grain boundaries of PNM91 after cycling, accompanied by Ni reduction (Figure 5d). This is closely correlated with rock salt formation due to the contact with the electrolyte, which is commonly observed in Ni-rich layered oxide cathodes.

On the other hand, numerous microcracks and voids are observed in cycled SNM91 (Figure 5e and Supporting Figures 26, 27). The voids existing in SC particles provide direct evidence of oxygen release from the lattice. High-resolution TEM images (Supporting Figure 28) with selected-area diffraction demonstrated that the particle surface was almost transformed into rock salt. An additional inactive rock salt phase is formed near the microcracks and at the voids inside the particles after 100 cycles (Figure 5f and Supporting Figure 29). This indicates that oxygen release not only occurred on the surface but also extended into the bulk. The GPA reveals significant lattice distortions around the microcracks, suggesting that severe lattice strain accumulation contributes to mechanical degradation within SC particles (Figure 5g). EELS mapping and line scan of the selected areas (Figure 5h and Supporting Figure 30) further reveal oxygen and Ni loss as well as Ni reduction at both the surface and microcrack regions of SNM91.

Based on the previous discussion, PNM91 exhibits more surface side reactions but experiences less transition-metal dissolution and demonstrates superior cycling performance compared to SNM91. This suggests that the degradation of SNM91 is primarily driven by bulk instability. The distinct Ni redox behaviors in these two cathodes significantly influence their structural stability as demonstrated in Figure 5i. In PNM91, composed of numerous nanosized primary particles within larger secondary particles, reactions tend to be heterogeneous across the particle. During delithiation, anisotropic lattice changes in PNM91 induce grain-boundary separation, allowing electrolyte penetration into the particle interior and facilitating delithiation in the bulk. The abrupt lattice contraction at high SoC increases contact with the electrolyte, which helps mitigate the impact of slow Li diffusion and promotes the homogeneous structure. Consequently, over extended cycling, phase transformations from a layered to rock salt structure occur not only at the particle surface but also near grain boundaries. Nonetheless, each of the primary particles maintains good structural integrity due to mitigated lattice strain. For SNM91, the reaction is relatively homogeneous at low SoC within each particle, which is unlikely to hinder kinetics or impact its performance due to the similar lattice parameters of the H1, M, and H2 phases. However, at high SoC, the formation of the H3 phase (a more-contracted layered structure) hinders the Li diffusion significantly, as the particle surface acts as the primary pathway for delithiation. As a result, the reaction tends to be more heterogeneous at high SoC, which leads to a wide distribution of the Ni valence state and triggers O redox activity due to the localized charge compensation between high-valence Ni and O. Moreover, the coexistence of H2 and H3 phases indicates the presence of lattice strain. The additional O redox, together with strain accumulation, exacerbates structural integrity by triggering microcrack formation, oxygen loss, and phase transformation over long-term cycling. These irreversible changes in both chemical and mechanical structures undermine structural stability and accelerating degradation.

Designing hybrid NMC particle architectures that combine the advantageous features of PC and SC structures could enhance the mechanical strength, energy density, and long-term stability. For instance, integrating the grain-boundary-like structure of PC materials with a high tap density and robustness of single crystals could create a synergistic structure that mitigates strain while increasing the volumetric energy density.

3. CONCLUSION

Overall, this study offers a comprehensive understanding of how the Ni redox behavior influences the electrochemical performance and chemomechanical degradation of Ni-rich layered oxide cathodes, focusing on both PC and SC morphologies. We examined the phase transformations and Ni oxidation behaviors for PNM91 and SNM91 using in situ

https://doi.org/10.1021/jacs.5c18922
J. Am. Chem. Soc. XXXX, XXX, XXX−XXX

XRD and XAS, revealing distinct relationships between chemical stability, phase evolution, and structural integrity in these two cathodes. 3D TXM-XANES imaging and GPA analysis show the grain-boundary architecture in PNM91 helps mitigate strain accumulation inside single primary particles by facilitating a uniform Ni redox process during cycling. However, SNM91 exhibits increasing structural heterogeneity at high SoC due to the kinetic limitation associated with its longer diffusion length. The pronounced chemical heterogeneity in SNM91 leads to the earlier oxygen redox activation and oxygen loss, which promotes irreversible phase transformation to the rock salt phase, generates microcracks, and exacerbates structural degradation. Meanwhile, we demonstrate the coevolution of interlayer strain and TM layer degradation leads to mechanical failures in SC Ni-rich cathode materials. Our studies have shed new light on microstructural and chemical evolution in Ni-rich layered oxides driven by different morphologies and offer insights into the performance gap between them, paving the way for more durable, high-energy-density batteries.

■ ASSOCIATED CONTENT

Supporting Information

The Supporting Information is available free of charge at https://pubs.acs.org/doi/10.1021/jacs.5c18922.

Additional experimental details and methods; supporting electrochemical data for all materials; additional figures supporting structure analyses including Li residue titration, SEM, TEM, XRD, and XAS data; and supporting tables summarizing fitting parameters from XRD and XAS (PDF)

■ AUTHOR INFORMATION

Corresponding Authors

Tongchao Liu − *Chemical Sciences and Engineering Division, Argonne National Laboratory, Lemont, Illinois 60439, United States; Pritzker School of Molecular Engineering, University of Chicago, Chicago, Illinois 60637, United States;* orcid.org/0000-0002-6010-3891; Email: liut@anl.gov.

Ying Shirley Meng − *Pritzker School of Molecular Engineering, University of Chicago, Chicago, Illinois 60637, United States; Argonne Collaborative Center for Energy Storage Science (ACCESS), Argonne National Laboratory, Lemont, Illinois 60439, United States;* orcid.org/0000-0001-8936-8845; Email: shirleymeng@uchicago.edu.

Khalil Amine − *Chemical Sciences and Engineering Division, Argonne National Laboratory, Lemont, Illinois 60439, United States; Pritzker School of Molecular Engineering, University of Chicago, Chicago, Illinois 60637, United States;* orcid.org/0000-0001-9206-3719; Email: amine@anl.gov.

Authors

Jing Wang − *Pritzker School of Molecular Engineering, University of Chicago, Chicago, Illinois 60637, United States; Chemical Sciences and Engineering Division, Argonne National Laboratory, Lemont, Illinois 60439, United States;* orcid.org/0000-0003-3684-3643

Jinghao Huang − *Center for Nanoscale Materials, Argonne National Laboratory, Lemont, Illinois 60439, United States*

Weiyuan Huang − *Chemical Sciences and Engineering Division, Argonne National Laboratory, Lemont, Illinois 60439, United States*

Haozhe Zhang − *Pritzker School of Molecular Engineering, University of Chicago, Chicago, Illinois 60637, United States; Chemical Sciences and Engineering Division, Argonne National Laboratory, Lemont, Illinois 60439, United States*

Tao Zhou − *Center for Nanoscale Materials, Argonne National Laboratory, Lemont, Illinois 60439, United States;* orcid.org/0000-0002-8093-7666

Qijia Zhu − *Chemical Sciences and Engineering Division, Argonne National Laboratory, Lemont, Illinois 60439, United States*

Jingtian Yang − *Pritzker School of Molecular Engineering, University of Chicago, Chicago, Illinois 60637, United States; Chemical Sciences and Engineering Division, Argonne National Laboratory, Lemont, Illinois 60439, United States*

Tianyi Li − *X-ray Science Division, Advanced Photon Sources, Argonne National Laboratory, Lemont, Illinois 60439, United States;* orcid.org/0000-0002-6234-6096

Lu Ma − *National Synchrotron Light Source II, Brookhaven National Laboratory, Upton, New York 11973, United States*

Xianghui Xiao − *National Synchrotron Light Source II, Brookhaven National Laboratory, Upton, New York 11973, United States;* orcid.org/0000-0002-7142-3452

Zengqing Zhuo − *Advanced Light Source, Lawrence Berkeley National Laboratory, Berkeley, California 94720, United States;* orcid.org/0000-0001-6602-760X

Jihyeon Gim − *Chemical Sciences and Engineering Division, Argonne National Laboratory, Lemont, Illinois 60439, United States;* orcid.org/0000-0002-4171-3707

Gangbin Yan − *Pritzker School of Molecular Engineering, University of Chicago, Chicago, Illinois 60637, United States;* orcid.org/0000-0002-4711-9063

Xiaozhou Huang − *Chemical Sciences and Engineering Division, Argonne National Laboratory, Lemont, Illinois 60439, United States*

Matthew Li − *Chemical Sciences and Engineering Division, Argonne National Laboratory, Lemont, Illinois 60439, United States;* orcid.org/0000-0001-9093-3207

Rachid Amine − *Material Science Division, Argonne National Laboratory, Lemont, Illinois 60439, United States*

Jianguo Wen − *Center for Nanoscale Materials, Argonne National Laboratory, Lemont, Illinois 60439, United States;* orcid.org/0000-0002-3755-0044

Complete contact information is available at: https://pubs.acs.org/10.1021/jacs.5c18922

Notes

The authors declare no competing financial interest.

■ ACKNOWLEDGMENTS

This work gratefully acknowledges support from the U.S. Department of Energy (DOE), Office of Energy Efficiency and Renewable Energy, Vehicle Technologies Office. Argonne National Laboratory is operated for DOE, Office of Science by UChicago Argonne, LLC, under Contract No. DE-AC02-06CH11357. Work performed at the Center for Nanoscale Materials and Advanced Photon Source (17-BM and 11-ID-C) and both US DOE Office of Science User Facilities was supported by the US DOE, Office of Basic Energy Sciences, under Contract No. DE-AC02-06CH11357. Use of the

National Synchrotron Light Source II (Beamlines 7-BM, 18-ID, and 28ID-2) is supported by the US DOE Office of Science User Facility operated by Brookhaven National Laboratory under Contract No. DE-SC0012704. This research used resources of the Advanced Light Source (Beamline 8.0.1), supported by the U.S. DOE Office of Science User Facility under Contract No. DE-AC02-05CH11231. Y.S.M. and J.Wang acknowledge the support from Energy Transition Network in the Istitude for Climate and Sustainable Growth at the University of Chicago. Y.S.M. and J.Wang acknowledge the startup funding from the Pritzker School of Molecular Engineering in University of Chicago that supported J.Wang's full graduate fellowship.

REFERENCES

(1) Deng, J.; Bae, C.; Denlinger, A.; Miller, T. Electric vehicles batteries: requirements and challenges. *Joule* **2020**, *4* (3), 511−515.
(2) Khan, F. N. U.; Rasul, M. G.; Sayem, A.; Mandal, N. Maximizing energy density of lithium-ion batteries for electric vehicles: A critical review. *Energy Rep.* **2023**, *9*, 11−21.
(3) Ding, Y.; Cano, Z. P.; Yu, A.; Lu, J.; Chen, Z. Automotive Li-ion batteries: current status and future perspectives. *Electrochem. Energy Rev.* **2019**, *2*, 1−28.
(4) Yan, Y.; Chen, D.; Sun, Z.; Zheng, Q.; Li, W.; Xue, J.; Chen, Y.; Wang, C.; Wang, C. W.; Liao, H. G.; et al.*et al.* Converting and fabricating $LiCoO_2$ cathode material into a disordered rocksalt surface modification layer to enhance interfacial stability of high-voltage cathode. *Angew. Chem.* **2025**, *137* (39), No. e202512300.
(5) Sun, Z.; Pan, J.; Chen, W.; Chen, H.; Zhou, S.; Wu, X.; Wang, Y.; Kim, K.; Li, J.; Liu, H.; et al.*et al.* Electrochemical processes and reactions in rechargeable battery materials revealed via in situ transmission electron microscopy. *Adv. Energy Mater.* **2024**, *14* (2), No. 2303165.
(6) Choi, J. U.; Voronina, N.; Sun, Y. K.; Myung, S. T. Recent progress and perspective of advanced high-energy Co-less Ni-rich cathodes for Li-ion batteries: yesterday, today, and tomorrow. *Adv. Energy Mater.* **2020**, *10* (42), No. 2002027.
(7) Wang, X.; Ding, Y. L.; Deng, Y. P.; Chen, Z. Ni-rich/Co-poor layered cathode for automotive Li-ion batteries: promises and challenges. *Adv. Energy Mater.* **2020**, *10* (12), No. 1903864.
(8) Li, M.; Lu, J.; Chen, Z.; Amine, K. 30 years of lithium-ion batteries. *Adv. Mater.* **2018**, *30* (33), No. 1800561.
(9) Liang, L.; Su, M.; Sun, Z.; Wang, L.; Hou, L.; Liu, H.; Zhang, Q.; Yuan, C. High-entropy doping promising ultrahigh-Ni Co-free single-crystalline cathode toward commercializable high-energy lithium-ion batteries. *Sci. Adv.* **2024**, *10* (25), No. eado4472.
(10) Li, L.; Fu, L.; Li, M.; Wang, C.; Zhao, Z.; Xie, S.; Lin, H.; Wu, X.; Liu, H.; Zhang, L.; et al.*et al.* B-doped and La_4NiLiO_8-coated Ni-rich cathode with enhanced structural and interfacial stability for lithium-ion batteries. *J. Energy Chem.* **2022**, *71*, 588−594.
(11) Kim, J.; Lee, H.; Cha, H.; Yoon, M.; Park, M.; Cho, J. Prospect and reality of Ni-rich cathode for commercialization. *Adv. Energy Mater.* **2018**, *8* (6), No. 1702028.
(12) Xia, Y.; Zheng, J.; Wang, C.; Gu, M. Designing principle for Ni-rich cathode materials with high energy density for practical applications. *Nano Energy* **2018**, *49*, 434−452.
(13) Ni, L.; Zhang, S.; Di, A.; Deng, W.; Zou, G.; Hou, H.; Ji, X. Challenges and strategies towards single-crystalline Ni-rich layered cathodes. *Adv. Energy Mater.* **2022**, *12* (31), No. 2201510.
(14) Zhang, H.; He, X.; Chen, Z.; Yang, Y.; Xu, H.; Wang, L.; He, X. Single-Crystalline Ni-Rich $LiNi_xMn_yCo_{1-x-y}O_2$ Cathode Materials: A Perspective. *Adv. Energy Mater.* **2022**, *12* (45), No. 2202022.
(15) You, B.; Wang, Z.; Shen, F.; Chang, Y.; Peng, W.; Li, X.; Guo, H.; Hu, Q.; Deng, C.; Yang, S.; et al.*et al.* Research progress of single-crystal nickel-rich cathode materials for lithium ion batteries. *Small Methods* **2021**, *5* (8), No. 2100234.
(16) Langdon, J.; Manthiram, A. A perspective on single-crystal layered oxide cathodes for lithium-ion batteries. *Energy Storage Mater.* **2021**, *37*, 143−160.
(17) Cha, H.; Kim, J.; Lee, H.; Kim, N.; Hwang, J.; Sung, J.; Yoon, M.; Kim, K.; Cho, J. Boosting reaction homogeneity in high-energy lithium-ion battery cathode materials. *Adv. Mater.* **2020**, *32* (39), No. 2003040.
(18) Han, Y.; Lei, Y.; Ni, J.; Zhang, Y.; Geng, Z.; Ming, P.; Zhang, C.; Tian, X.; Shi, J. L.; Guo, Y. G.; Xiao, Q. Single-crystalline cathodes for advanced Li-ion batteries: progress and challenges. *Small* **2022**, *18* (43), No. 2107048.
(19) Li, H.; Li, J.; Ma, X.; Dahn, J. Synthesis of single crystal $LiNi_{0.6}Mn_{0.2}Co_{0.2}O_2$with enhanced electrochemical performance for lithium ion batteries. *J. Electrochem. Soc.* **2018**, *165* (5), A1038−A1045.
(20) Qian, G.; Zhang, Y.; Li, L.; Zhang, R.; Xu, J.; Cheng, Z.; Xie, S.; Wang, H.; Rao, Q.; He, Y.; et al.*et al.* Single-crystal nickel-rich layered-oxide battery cathode materials: synthesis, electrochemistry, and intragranular fracture. *Energy Storage Mater.* **2020**, *27*, 140−149.
(21) Li, J.; Cameron, A. R.; Li, H.; Glazier, S.; Xiong, D.; Chatzidakis, M.; Allen, J.; Botton, G.; Dahn, J. Comparison of single crystal and polycrystalline $LiNi_{0.5}Mn_{0.3}Co_{0.2}O_2$ positive electrode materials for high voltage Li-ion cells. *J. Electrochem. Soc.* **2017**, *164* (7), No. A1534.
(22) Li, J.; Li, H.; Stone, W.; Glazier, S.; Dahn, J. Development of electrolytes for single crystal NMC532/artificial graphite cells with long lifetime. *J. Electrochem. Soc.* **2018**, *165* (3), A626.
(23) Hu, J.; Li, L.; Bi, Y.; Tao, J.; Lochala, J.; Liu, D.; Wu, B.; Cao, X.; Chae, S.; Wang, C.; Xiao, J. Locking oxygen in lattice: A quantifiable comparison of gas generation in polycrystalline and single crystal Ni-rich cathodes. *Energy Storage Mater.* **2022**, *47*, 195−202.
(24) Teichert, P.; Jahnke, H.; Figgemeier, E. Degradation mechanism of monocrystalline Ni-rich $Li[Ni_xMn_yCo_z]O_2$ (NMC) active material in lithium ion batteries. *J. Electrochem. Soc.* **2021**, *168* (9), No. 090532.
(25) Ryu, H.-H.; Namkoong, B.; Kim, J.-H.; Belharouak, I.; Yoon, C. S.; Sun, Y.-K. Capacity fading mechanisms in Ni-rich single-crystal NCM cathodes. *ACS Energy Lett.* **2021**, *6* (8), 2726−2734.
(26) Huang, W.; Liu, T.; Yu, L.; Wang, J.; Zhou, T.; Liu, J.; Li, T.; Amine, R.; Xiao, X.; Ge, M.; et al.*et al.* Unrecoverable lattice rotation governs structural degradation of single-crystalline cathodes. *Science* **2024**, *384* (6698), 912−919.
(27) Yan, P.; Zheng, J.; Gu, M.; Xiao, J.; Zhang, J.-G.; Wang, C.-M. Intragranular cracking as a critical barrier for high-voltage usage of layer-structured cathode for lithium-ion batteries. *Nat. Commun.* **2017**, *8* (1), No. 14101.
(28) Liang, L.; Zhang, W.; Zhao, F.; Denis, D. K.; Zaman, F. U.; Hou, L.; Yuan, C. Surface/interface structure degradation of Ni-rich layered oxide cathodes toward lithium-ion batteries: fundamental mechanisms and remedying strategies. *Adv. Mater. Interfaces* **2020**, *7* (3), No. 1901749.
(29) Kim, J.; Cha, H.; Lee, H.; Oh, P.; Cho, J. Surface and interfacial chemistry in the nickel-rich cathode materials. *Batteries Supercaps* **2020**, *3* (4), 309−322.
(30) Xu, C.; Märker, K.; Lee, J.; Mahadevegowda, A.; Reeves, P. J.; Day, S. J.; Groh, M. F.; Emge, S. P.; Ducati, C.; Layla Mehdi, B.; et al.*et al.* Bulk fatigue induced by surface reconstruction in layered Ni-rich cathodes for Li-ion batteries. *Nat. Mater.* **2021**, *20* (1), 84−92.
(31) Kim, J.-M.; Zhang, X.; Zhang, J.-G.; Manthiram, A.; Meng, Y. S.; Xu, W. A review on the stability and surface modification of layered transition-metal oxide cathodes. *Mater. Today* **2021**, *46*, 155−182.
(32) Ryu, H.-H.; Park, K.-J.; Yoon, C. S.; Sun, Y.-K. Capacity fading of Ni-rich Li $[Ni_xCo_yMn_{1-x-y}]O_2$ ($0.6 \leq x \leq 0.95$) cathodes for high-energy-density lithium-ion batteries: bulk or surface degradation? *Chem. Mater.* **2018**, *30* (3), 1155−1163.
(33) Yin, S.; Deng, W.; Chen, J.; Gao, X.; Zou, G.; Hou, H.; Ji, X. Fundamental and solutions of microcrack in Ni-rich layered oxide

https://doi.org/10.1021/jacs.5c18922
J. Am. Chem. Soc. XXXX, XXX, XXX−XXX

cathode materials of lithium-ion batteries. *Nano Energy* **2021**, *83*, No. 105854.
(34) Wu, F.; Liu, N.; Chen, L.; Su, Y.; Tan, G.; Bao, L.; Zhang, Q.; Lu, Y.; Wang, J.; Chen, S.; Tan, J. Improving the reversibility of the H2-H3 phase transitions for layered Ni-rich oxide cathode towards retarded structural transition and enhanced cycle stability. *Nano energy* **2019**, *59*, 50−57.
(35) Fan, X.; Ou, X.; Zhao, W.; Liu, Y.; Zhang, B.; Zhang, J.; Zou, L.; Seidl, L.; Li, Y.; Hu, G.; et al.*et al.* In situ inorganic conductive network formation in high-voltage single-crystal Ni-rich cathodes. *Nat. Commun.* **2021**, *12* (1), No. 5320.
(36) Liu, T.; Yu, L.; Liu, J.; Lu, J.; Bi, X.; Dai, A.; Li, M.; Li, M.; Hu, Z.; Ma, L.; et al. Understanding Co roles towards developing Co-free Ni-rich cathodes for rechargeable batteries. *Nat. Energy* **2021**, *6* (3), 277−286.
(37) Zhang, J.-N.; Li, Q.; Ouyang, C.; Yu, X.; Ge, M.; Huang, X.; Hu, E.; Ma, C.; Li, S.; Xiao, R. Trace doping of multiple elements enables stable battery cycling of $LiCoO_2$ at 4.6 V. *Nat. Energy* **2019**, *4* (7), 594−603.
(38) Mu, L.; Yang, Z.; Tao, L.; Waters, C. K.; Xu, Z.; Li, L.; Sainio, S.; Du, Y.; Xin, H. L.; Nordlund, D.; Lin, F. The sensitive surface chemistry of Co-free, Ni-rich layered oxides: identifying experimental conditions that influence characterization results. *J. Mater. Chem. A* **2020**, *8* (34), 17487−17497.
(39) Malik, M.; Chan, K. H.; Azimi, G. Review on the synthesis of $LiNi_xMn_yCo_{1-x-y}O_2$ (NMC) cathodes for lithium-ion batteries. *Mater. Today Energy* **2022**, *28*, No. 101066.
(40) Entwistle, T.; Sanchez-Perez, E.; Murray, G. J.; Anthonisamy, N.; Cussen, S. A. Co-precipitation synthesis of nickel-rich cathodes for Li-ion batteries. *Energy Rep.* **2022**, *8*, 67−73.
(41) Liu, T.; Yu, L.; Lu, J.; Zhou, T.; Huang, X.; Cai, Z.; Dai, A.; Gim, J.; Ren, Y.; Xiao, X.; et al.*et al.* Rational design of mechanically robust Ni-rich cathode materials via concentration gradient strategy. *Nat. Commun.* **2021**, *12* (1), No. 6024.
(42) Jiang, M.; Danilov, D. L.; Eichel, R. A.; Notten, P. H. A review of degradation mechanisms and recent achievements for Ni-rich cathode-based Li-ion batteries. *Adv. Energy Mater.* **2021**, *11* (48), No. 2103005.
(43) Yu, H.; Zhu, H.; Jiang, H.; Su, X.; Hu, Y.; Jiang, H.; Li, C. Restraining the escape of lattice oxygen enables superior cyclic performance towards high-voltage Ni-rich cathodes. *Nat. Sci. Rev.* **2023**, *10* (1), No. nwac166.
(44) Li, N.; Sallis, S.; Papp, J. K.; Wei, J.; McCloskey, B. D.; Yang, W.; Tong, W. Unraveling the cationic and anionic redox reactions in a conventional layered oxide cathode. *ACS Energy Lett.* **2019**, *4* (12), 2836−2842.
(45) Xu, J.; Sun, M.; Qiao, R.; Renfrew, S. E.; Ma, L.; Wu, T.; Hwang, S.; Nordlund, D.; Su, D.; Amine, K.; et al.*et al.* Elucidating anionic oxygen activity in lithium-rich layered oxides. *Nat. Commun.* **2018**, *9* (1), No. 947.
(46) Yang, T.; Zhang, K.; Zuo, Y.; Song, J.; Yang, Y.; Gao, C.; Chen, T.; Wang, H.; Xiao, W.; Jiang, Z.; Xia, D. Ultrahigh-nickel layered cathode with cycling stability for sustainable lithium-ion batteries. *Nat. Sustainability* **2024**, *7* (9), 1204−1214.
(47) Cheng, X.; Zheng, J.; Lu, J.; Li, Y.; Yan, P.; Zhang, Y. Realizing superior cycling stability of Ni-Rich layered cathode by combination of grain boundary engineering and surface coating. *Nano Energy* **2019**, *62*, 30−37.
(48) Sharifi-Asl, S.; Yurkiv, V.; Gutierrez, A.; Cheng, M.; Balasubramanian, M.; Mashayek, F.; Croy, J.; Shahbazian-Yassar, R. Revealing grain-boundary-induced degradation mechanisms in Li-rich cathode materials. *Nano Lett.* **2020**, *20* (2), 1208−1217.
(49) Wang, J.; Liu, T.; Huang, W.; Yu, L.; Zhang, H.; Zhou, T.; Li, T.; Huang, X.; Xiao, X.; Ma, L.; Holt, M. V.; Ryu, K.; Amine, R.; Xu, W.; Li, L.; Wen, J.; Meng, Y. S.; Amine, K. Nanoscopic strain evolution in single-crystal battery positive electrodes. *Nat. Nanotechnol.* **2026**, *21*, 229−239.

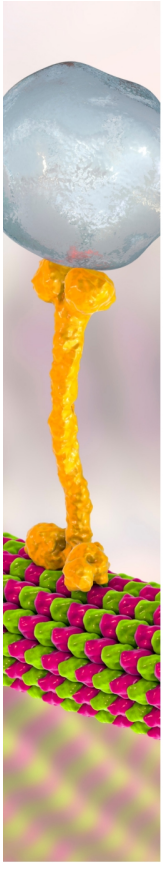

https://doi.org/10.1021/jacs.5c18922
J. Am. Chem. Soc. XXXX, XXX, XXX−XXX